

Iris Segmentation Using Geodesic Active Contours

Samir Shah and Arun Ross, *Member, IEEE*

Abstract—The richness and apparent stability of the iris texture make it a robust biometric trait for personal authentication. The performance of an automated iris recognition system is affected by the accuracy of the segmentation process used to localize the iris structure. Most segmentation models in the literature assume that the pupillary, limbic, and eyelid boundaries are circular or elliptical in shape. Hence, they focus on determining model parameters that best fit these hypotheses. However, it is difficult to segment iris images acquired under nonideal conditions using such conic models. In this paper, we describe a novel iris segmentation scheme employing geodesic active contours (GACs) to extract the iris from the surrounding structures. Since active contours can 1) assume any shape and 2) segment multiple objects simultaneously, they mitigate some of the concerns associated with traditional iris segmentation models. The proposed scheme elicits the iris texture in an iterative fashion and is guided by both local and global properties of the image. The matching accuracy of an iris recognition system is observed to improve upon application of the proposed segmentation algorithm. Experimental results on the CASIA v3.0 and WVU nonideal iris databases indicate the efficacy of the proposed technique.

Index Terms—Geodesic active contours (GACs), iriscodes, iris recognition, iris segmentation, level sets, snakes.

I. INTRODUCTION

THE iris is an internal organ of the eye that is located just behind the cornea and in front of the lens. Its function is to control the size of the pupil, which in turn regulates the amount of light entering the pupil and impinging the retina. Flom and Safir [1] have postulated that “the basic, significant features of the iris remain extremely stable and do not change over a period of many years” (this claim has been challenged in the recent literature). They state that every iris is unique and no two individuals have the same iris compositions. Indeed, the two irides of an individual have been observed to be different in their intricate texture structure. Hence, the iris is considered to be a robust and unique biometric with a very low False Accept Rate (FAR). Large-scale authentication experiments have confirmed this notion further underscoring the relevance of this biometric trait in distinguishing individuals [2], [3].

Manuscript received June 29, 2008; revised July 11, 2009. First published September 29, 2009. This work was supported in part by the Center for Identification Technology Research (CITeR) at West Virginia University and in part by the NSF CAREER Award IIS 0642554. A preliminary version of this work was presented at the 2006 Biometrics Symposium, Baltimore, MD, Sep. 2006. The associate editor coordinating the review of this manuscript and approving it for publication was Dr. Tieniu Tan.

S. Shah is with the Iris Technology Division, LG Electronics USA Inc., Cranbury, NJ 08512 USA (e-mail: sshahd@gmail.com).

A. Ross is with West Virginia University, Morgantown, WV 26506 USA (e-mail: Arun.Ross@mail.wvu.edu).

Color versions of one or more of the figures in this paper are available online at <http://ieeexplore.ieee.org>.

Digital Object Identifier 10.1109/TIFS.2009.2033225

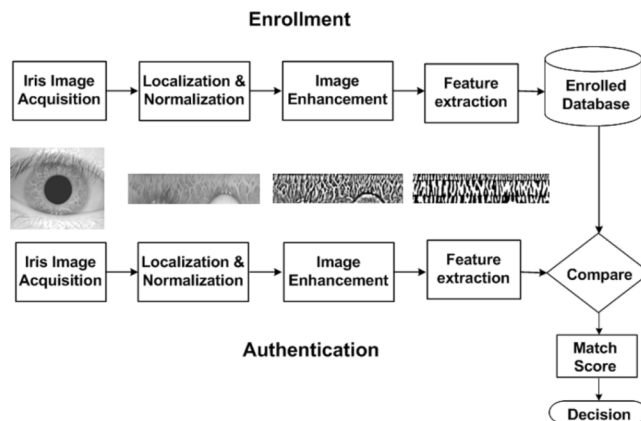


Fig. 1. Block diagram of an iris recognition system.

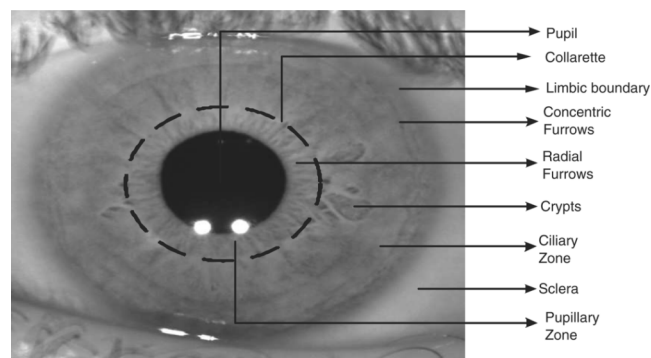


Fig. 2. Salient features in the anterior portion of the iris.

The function of an iris recognition system is to extract, represent and compare the textural intricacy present on the surface of the iris. Such a system comprises of modules for iris segmentation, enhancement, feature extraction (encoding) and feature matching (Fig. 1). The first and, perhaps, the most important step in an iris recognition system is iris segmentation or localization. Segmentation involves detecting and isolating the iris structure from an image of the eye. As seen in Fig. 2, the iris projected onto a 2-D plane appears to be located in the vicinity of the sclera, pupil, and eyelids. Thus, the segmentation process has to accurately detect boundaries separating the iris from these components. Apart from estimating the actual shape of the iris, the segmentation routine should detect occlusions due to eyelashes that can confound the extracted features. Errors in segmentation may result in inferior recognition performance due to inaccurate encoding of the textural content of the iris.

Several iris recognition algorithms have been proposed in the literature. Daugman [4], [5] uses a texture-based method to encode irides. Multiscale 2-D Gabor-Wavelet transform is used to generate a 256-byte iriscodes. Hamming distance is then used as a measure to determine the proximity of two iriscodes. The

TABLE I

EXAMPLES OF A FEW IRIS SEGMENTATION, ENCODING AND MATCHING TECHNIQUES PROPOSED IN THE LITERATURE. OTHER EXAMPLES CAN BE FOUND IN [2]

Authors	Segmentation Technique	Encoding Technique	Matching Technique
Daugman [4]	Integro-differential operator	Multiscale 2-D Gabor Wavelet coefficients	Hamming distance
Wildes [6]	Edge detection and Hough transform	Laplacian-of-a-Gaussian (LOG) filter	Normalized correlation
Bole and Boashash [18]	Edge and contour detection	Zero crossings of Wavelet transform	Dissimilarity function on the iris
Masek and Kovesi [7]	Edge detection and Hough transform	1D Log-Gabor filters	Hamming distance
Ma et al. [8]	Edge detection and Hough transform	Circular symmetric Gabor filters	Nearest feature line
Lim et al. [9]	Edge detection and Hough transform	2-D Haar Wavelet transform	Competitive learning neural network
Noh et al. [19]	No information about segmentation	ICA	Hamming distance
Ma et al. [10]	Edge detection and Hough transform	Key local variations using Wavelet transform	Exclusive OR operation
Huang et al. [11]	Edge detection and Hough transform	Bank of Log-Gabor filters	Euclidean distance
Huang et al. [15]	Phase congruency and Hough transform	Multiscale 2-D Gabor Wavelet coefficients	Hamming distance
Yuan et al. [12]	Edge detection and Hough transform	2-D phase congruency	Euclidean distance
Dorairaj et al. [20]	Integro-differential operator	PCA and ICA	Euclidean distance
Thornton et al. [14]	Hough transform	Advanced correlation filter	Advanced correlation filter
He et al. [21], [22]	Pulling and pushing elastic model	Regional ordinal measure	Hamming distance
Abhyankar and Schuckers [16]	Active Shape Models	Bi-orthogonal Wavelet	Hamming distance

integro-differential operator, which acts as a circular edge detector, is employed for determining the inner and outer boundaries of the iris as well as the upper and lower eyelids. Wildes [6] uses Laplacian-of-a-Gaussian (LOG) filter to extract features from the iris image. A Hough transform-based method is used to segment the iris. Also, the upper and lower boundaries of the eyelid are approximated using parabolic curves. Matching is done using the normalized correlation between the test and training images. Masek and Kovesi [7] employ weighted gradients using a combination of Kovesi's modified canny edge detector and the circular Hough-transform to segment the iris. Several other segmentation schemes proposed in the literature are also based on the Hough-transform (see, for example, [8]–[14]). Huang *et al.* [15] first coarsely segment the iris using edge detection filters and Hough transform before normalizing it. The noise due to eyelids is then localized by the edge information based on phase congruency. Abhyankar and Schuckers [16] use training based Active Shape Models to segment the iris from the sclera. The nonlinear shape of the iris is learned using a few training images. More recently, Daugman [3] designed novel segmentation and encoding schemes for processing nonideal irides. Hollingsworth [17] illustrated that every iriscode (iris template) has some *fragile* bits. A bit is fragile if it has a significant probability of being a 0 for some images of the iris and 1 for other images of the same iris. If the fragile bits were masked, the performance of the iris recognition system was observed to increase. Table I summarizes the segmentation, encoding (i.e., representation) and matching techniques of a few algorithms described in the literature.

Most segmentation models in the literature assume that the pupillary, the limbic, and the eyelid boundaries are circular or elliptical in shape. Hence, they focus on determining model parameters that best fit these hypotheses ([4], [6], [10]). Only very few algorithms in the literature do not assume circular or elliptical boundaries (e.g., see Abhyankar and Schuckers [16] and Daugman [3]). In this paper, a novel geodesic active contour (GAC)-based scheme is employed to accurately determine the boundary of the iris thereby eliciting the shape of its boundary. As the boundary of the iris is not approximated using a circle

or an ellipse in the proposed scheme, the localized iris region is expected to contain very few noniris pixels. Active Contours have been extensively used in the field of medical image analysis for segmenting various images like brain MRI images [23] and abdominal CT images [24]. They have also been used in the field of machine vision [25]. In this paper, their significance in the context of efficient iris segmentation is demonstrated.

The remainder of the paper is organized as follows. A baseline segmentation, encoding and matching method is described in Section II. Section III provides an overview of the proposed segmentation technique based on GACs. The matching performance due to this novel scheme is reported in Section IV. Section V concludes the paper.

II. BASELINE IRIS SEGMENTATION, ENCODING, AND MATCHING TECHNIQUE

In order to demonstrate the performance improvement obtained using the proposed algorithm, a baseline segmentation, encoding and matching algorithm is first defined. Integro-differential operators, which are a variation of the Hough transform, act as circular edge detectors and have been previously used to determine the inner and the outer boundaries of the iris. They also have been used to determine the elliptical boundaries of the lower and the upper eyelids. An integro-differential operator can be defined as $\max_{(r,x_0,y_0)} |G_\sigma(r) * (\partial)/(\partial r) \oint_{r,x_0,y_0} (I(x,y))/(2\pi r) ds|$ where $I(x,y)$ is the image, r is the radius of the pupil or iris, (x_0,y_0) its center and $G_\sigma(r)$ is the Gaussian smoothing function with scale σ . Thus, the integro-differential operator searches for a circular boundary with radius r and center (x_0,y_0) such that the change in radial pixel intensity across the boundary is maximum. The eyelids can be detected in a similar fashion by performing the integration on an elliptical boundary rather than a circular one. The output of the segmentation process is a binary mask that indicates the iris and noniris pixels in the image.

Iris segmentation is followed by a normalization scheme to generate a fixed dimension feature vector that lends itself to matching. Each point in the (x,y) domain is mapped to a pair

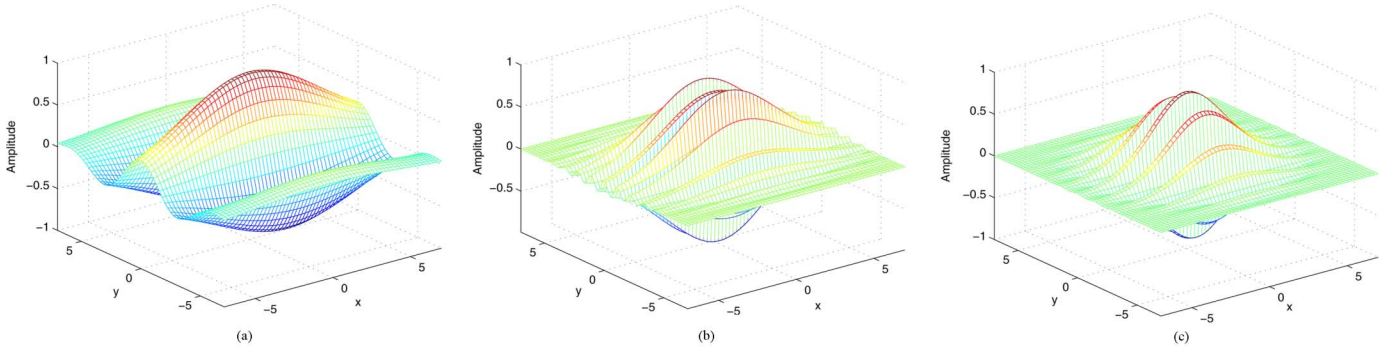


Fig. 3. Real part of 2-D Gabor wavelet filters.

of polar coordinates (r, θ) (like the rubber sheet model proposed by Daugman [4]). This results in a fixed size unwrapped rectangular iris image. Gabor filters are then used to extract the textural information from the unwrapped iris (encoding). A 2-D Gabor filter over an image domain (x, y) is given by $G(x, y) = e^{-\pi[(x-x_0)^2/\alpha^2+(y-y_0)^2/\beta^2]} e^{-2\pi i[u_0(x-x_0)+\nu_0(y-y_0)]}$ where (x_0, y_0) specifies the center of the Gaussian filter, α and β are the width and length of the filter, (u_0, ν_0) specify the modulation with frequency $\omega_0 = \sqrt{u_0^2 + \nu_0^2}$ and orientation $\theta = \arctan(\nu_0/u_0)$.¹ The prominence of the iris texture changes as one moves away from the pupil. Hence, a set of three Gabor filters with different scales and frequency but the same orientation (0°) are applied to different regions of the “normalized” iris as shown in Fig. 3. The filtering results in complex-valued phase information. This phase information is quantized into four quadrants in the complex plane resulting in two bits denoting the real and complex parts of the phasor response at a pixel. The resulting binary feature vector is called an iriscode. The difference between two such iriscodes is measured using the Hamming distance which is a measure of the number of different bits between the two iriscodes. The Hamming distance is a dissimilarity score and is calculated using the bits corresponding to the iris pixels by utilizing the binary masks generated in the segmentation process. Let I_1 and I_2 be the two iriscodes to be compared, and M_1 and M_2 be their respective masks. The Hamming distance (HD) is calculated as follows:

$$\text{HD} = \frac{\|(I_1 \otimes I_2) \cap M_1 \cap M_2\|}{\|M_1 \cap M_2\|}$$

where the XOR operator, \otimes , detects the disagreement between the corresponding bits in the iriscodes, the AND operator, \cap , ensures that the Hamming distance is calculated using only the bits generated from the true iris region and the $\|\cdot\|$ operator computes the norm of the bit vector. Ideally, the Hamming distance between two images of the same iris will be 0 (genuine score) and that between two images of different irides will be (0.5) (impostor score).

III. IRIS SEGMENTATION USING GACS

The iris localization procedure can be broadly divided into two stages: (a) pupil segmentation and (b) iris segmentation.

¹One could use a 1-D Gabor filter instead of a 2-D Gabor filter since the iris information does not change radially as much as it does angularly [26].

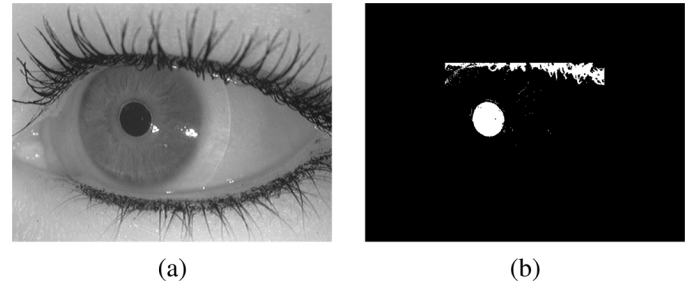


Fig. 4. Pupil binarization. (a) Image of an eye with dark eyelashes. (b) Thresholded binary iris image.

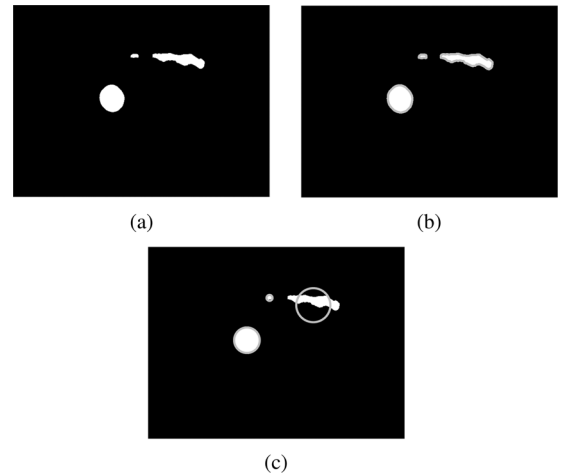


Fig. 5. Pupil Segmentation. (a) 2-D Median filtered binary iris image. (b) Traced boundaries of all the remaining objects in the binary image (shown in gray color). (c) Fitting circle on all potential regions where the pupil might be present (shown in gray).

A. Pupil Segmentation

To detect the pupillary boundary, the eye image is first smoothed using a 2-D median filter and the minimum pixel value (M) is determined. The iris is then binarized using a threshold value $25 + M$. Fig. 4(b) shows an iris image after binarization. As expected, apart from the pupil, other dark regions of the eye (e.g., eyelashes) fall below this threshold value. A 2-D median filter is then applied on the binary image to discard the relatively smaller regions associated with the eyelashes. This reduces the number of candidate iris pixels detected as a consequence of thresholding as seen in Fig. 5(a). Based on the median-filtered binary image, the exterior boundaries of all the remaining objects are traced as shown in Fig. 5(b). Generally, the largest boundary of the remaining

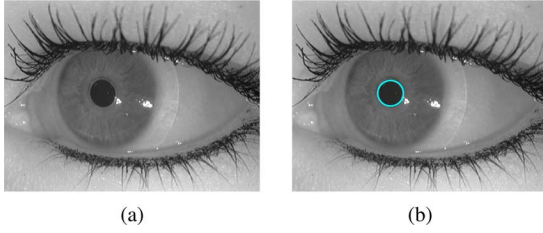


Fig. 6. Pupil segmentation. (a) Image of an eye with dark eyelashes. (b) Segmented pupil (shown in blue).

regions of the eye corresponds to the pupil. However, when the pupil is constricted, it is very likely that the boundary of the detected region corresponding to the eyelashes is larger than that of the pupil. So a circle-fitting procedure is executed on all detected regions. The equation of a circle is given by $x^2 + y^2 + a_1x + a_2y + a_3 = 0$ where (x, y) represent the coordinates of a point on the circle. The coordinates of the center can be computed as $x_0 = -a_1/2, y_0 = -a_2/2$ and the radius as $R_i = \sqrt{(a_1^2 + a_2^2)/4 - a_3}$. Let $\{(x_i, y_i) \mid i = 1, 2, \dots, n\}$ be n points traversed by the circle, and let

$$M = \begin{bmatrix} x_1^2 + y_1^2 \\ x_2^2 + y_2^2 \\ \dots \\ x_n^2 + y_n^2 \end{bmatrix}_{n \times 1}, N = \begin{bmatrix} x_1 & y_1 & 1 \\ x_2 & y_2 & 1 \\ \dots & \dots & \dots \\ x_n & y_n & 1 \end{bmatrix}_{n \times 3}$$

$$A = \begin{bmatrix} a_1 \\ a_2 \\ a_3 \end{bmatrix}_{3 \times 1}.$$

Then the equation of the circle may be written as $NA = M$. Thus, to estimate the radius and the center of the circle, the expression $A = N^{-1}M$ needs to be solved. Since N is not a square matrix, its inverse is computed using the least squares criterion.² Fig. 5(c) demonstrates the circles fitted through all the detected regions. Finally, the circle whose circumference contains the maximum number of black pixels is deemed to be the detected pupil. Regions with diameters more than half the image size are not considered. Fig. 6 shows an iris image containing dark eyelashes and the correctly segmented pupil using the aforementioned algorithm. Sometimes, specular reflections can occur near the boundary of the pupil that may confound the pupil segmentation procedure. For example, in Fig. 7, it is obvious that the pupil is under-segmented due to the presence of the specular reflection near the pupil boundary. Hence, if specular reflection (bright spots in an image) is detected in the vicinity of the pupil, it is “inpainted” using the surrounding information [27]. Inpainting is a process to fill in the missing portions of an image (in our case specular reflections) to improve its integrity [28]. Fig. 8(f) demonstrates that the pupil detection procedure is made more robust by inpainting those specular reflections in the iris image that occur near the pupil boundary. Since the specular reflections are detected by a simple image thresholding technique, other regions of the eye that are over-exposed to light may also be incorrectly detected. However, in-

painting such regions with the surrounding information will be beneficial.

Fig. 9 presents other results of the pupil segmentation process.

B. Iris Segmentation

To detect the limbic boundary of the iris, a novel scheme based on a level sets representation [29], [25] of the GAC model is employed. This approach is based on the relation between active contours and the computation of geodesics (minimal length curves) [30]. The technique is to evolve the contour from inside the iris under the influence of geometric measures of the iris image. GACs combine the energy minimization approach of the classical “snakes” and the geometric active contours based on curve evolution.

The proposed technique is significantly different from the one proposed by Daugman [3]. In [3], the active contour is defined as a Fourier boundary approximated using the coefficients of the Fourier series. The technique relies on the *order* of the Fourier series to approximate the inner and outer boundaries of the iris. Further, the order of the two boundaries is likely to be different (as pointed out in the paper). Thus, selecting the order of the Fourier series is an important task.

1) *GACs*: Let $\gamma(t)$ be the curve, that has to gravitate toward the boundary of any object, at a particular time t as shown in Fig. 10. The time t corresponds to the iteration number. Let ψ be a function defined as a signed distance function from the curve $\gamma(t)$. Thus, $\psi(x, y) = \text{distance of point } (x, y) \text{ to the curve } \gamma(t)$.

$$\psi(x, y) = \begin{cases} 0, & \text{if } (x, y) \text{ is on the curve} \\ < 0, & \text{if } (x, y) \text{ is inside the curve} \\ > 0, & \text{if } (x, y) \text{ is outside the curve.} \end{cases} \quad (1)$$

ψ is of the same dimension as that of the image $I(x, y)$ that is to be segmented. The curve $\gamma(t)$ is a level set of the function ψ . Level sets are the set of all points in ψ where $\psi = \text{some constant}$. Thus, $\psi = 0$ is the zeroth level set, $\psi = 1$ is the first level set and so on. ψ is the implicit representation of the curve $\gamma(t)$ and is called as the embedding function since it embeds the evolution of $\gamma(t)$. The embedding function evolves under the influence of image gradients and regions characteristics so that the curve $\gamma(t)$ approaches the boundary of the object. Thus, instead of evolving the parametric curve $\gamma(t)$ (e.g., the Lagrangian approach used in snakes), the embedding function itself is evolved. In our algorithm, the initial curve $\gamma(t)$ is assumed to be a circle of radius r just beyond the pupillary boundary. Let the curve $\gamma(t)$ be the zeroth-level set of the embedding function. This implies that

$$\frac{d\psi}{dt} = 0.$$

By the chain rule

$$\frac{d\psi}{dt} = \frac{\partial\psi}{\partial x} \frac{dx}{dt} + \frac{\partial\psi}{\partial y} \frac{dy}{dt} + \frac{\partial\psi}{\partial t}$$

i.e.,

$$\frac{\partial\psi}{\partial t} = -\nabla\psi \cdot \gamma'(t).$$

²[Online]. Available: <http://www.mathworks.com/moler/leastquares.pdf>

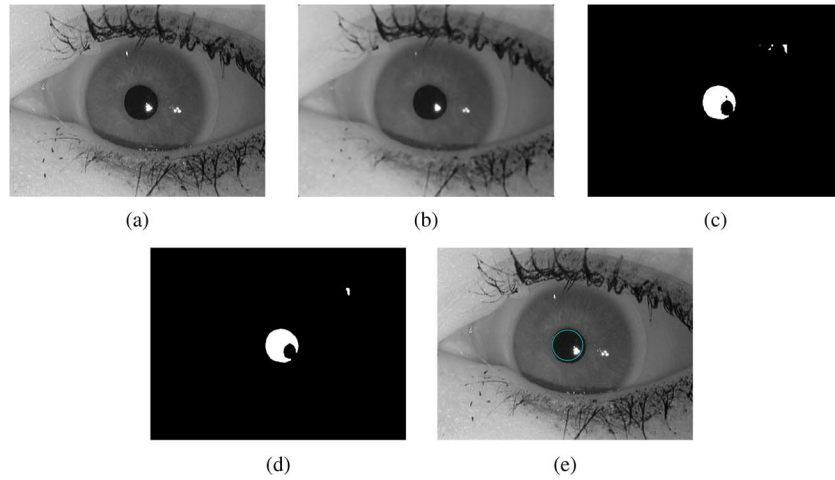


Fig. 7. Result of pupil segmentation when inpainting is not used to remove specular reflections. (a) Eye image. (b) Smoothed image. (c) Thresholded binary image. (d) 2-D Median filtered image. (e) Undersegmented pupil (shown using blue-colored contour).

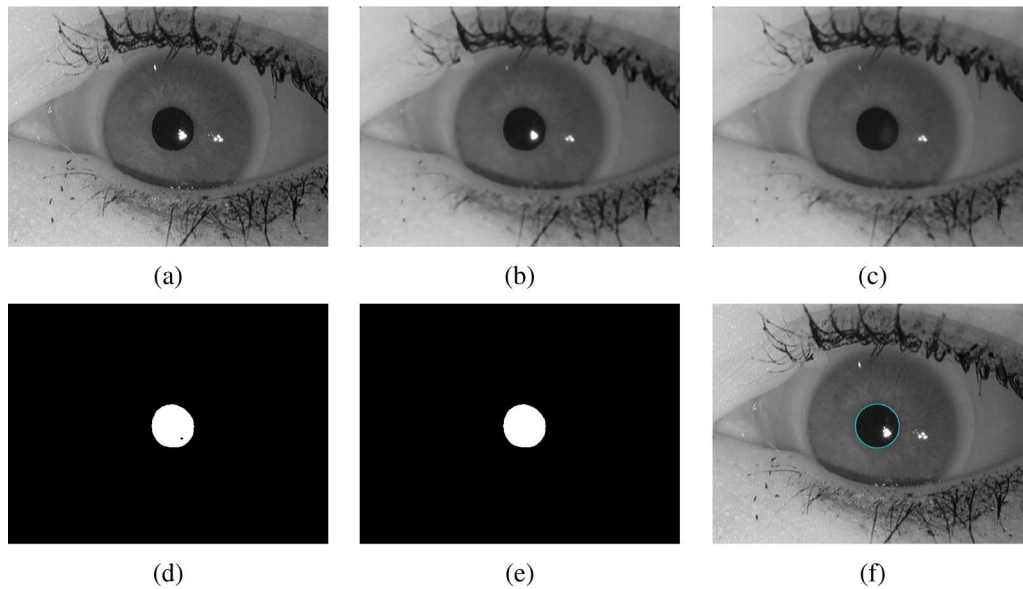


Fig. 8. Result of pupil segmentation when inpainting is used to remove specular reflections in the vicinity of the pupil. (a) Eye image. (b) Smoothed image. (c) Inpainted specular reflection in the vicinity of the pupil. (d) Thresholded binary image. (e) 2-D Median filtered image. (f) Segmented pupil (shown using blue-colored contour).

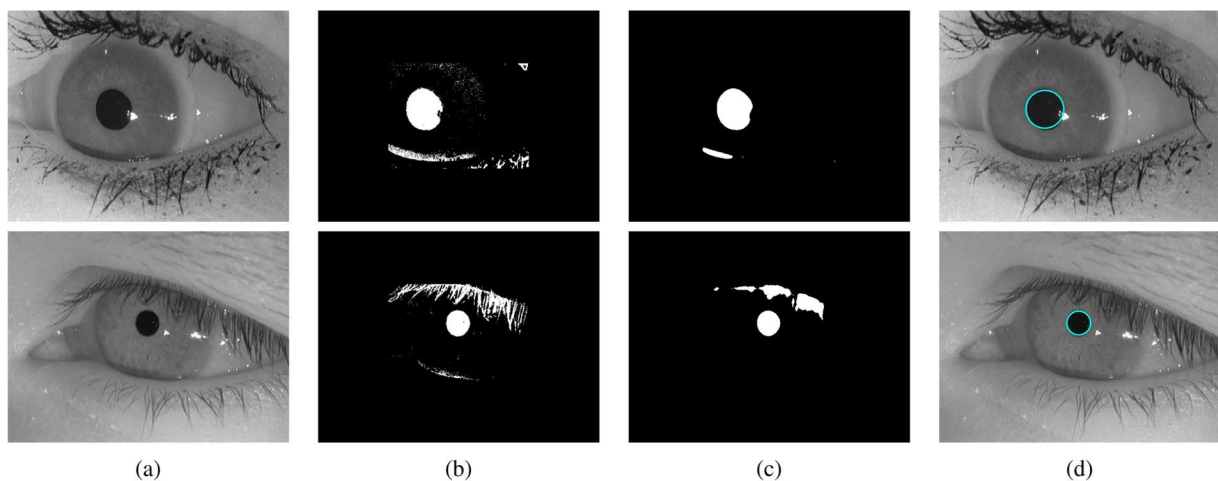
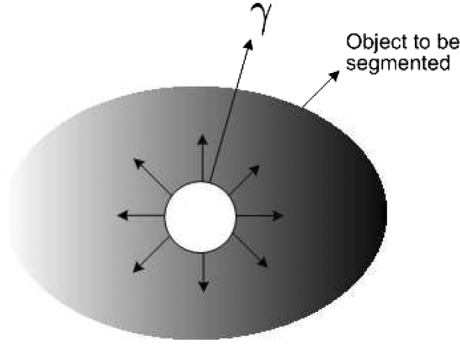


Fig. 9. Pupil segmentation. (a) Iris image. (b) Thresholded binary image. (c) 2-D Median filtered image. (d) Segmented pupil (shown using blue-colored contour).


 Fig. 10. Curve γ evolving towards the boundary of the object.

Splitting the $\gamma'(t)$ in the normal ($N(t)$) and tangential ($T(t)$) directions,

$$\frac{\partial \psi}{\partial t} = -\nabla \psi \cdot (v_N N(t) + v_T T(t)).$$

Now, since $\nabla \psi$ is perpendicular to the tangent to $\gamma(t)$

$$\frac{\partial \psi}{\partial t} = -\nabla \psi \cdot (v_N N(t)). \quad (2)$$

The normal component is given by

$$N = \frac{\nabla \psi}{\|\nabla \psi\|}.$$

Substituting this in (2)

$$\frac{\partial \psi}{\partial t} = -v_N \|\nabla \psi\|.$$

Let v_N be a function of the curvature of the curve κ , stopping function K (to stop the evolution of the curve) and the inflation force c (to evolve the curve in the outward direction) such that,

$$\frac{\partial \psi}{\partial t} = - \left(\text{div} \left(K \frac{\nabla \psi}{\|\nabla \psi\|} \right) + cK \right) \|\nabla \psi\|.$$

Thus, the evolution equation for ψ_t such that $\gamma(t)$ remains the zeroth level set is given by

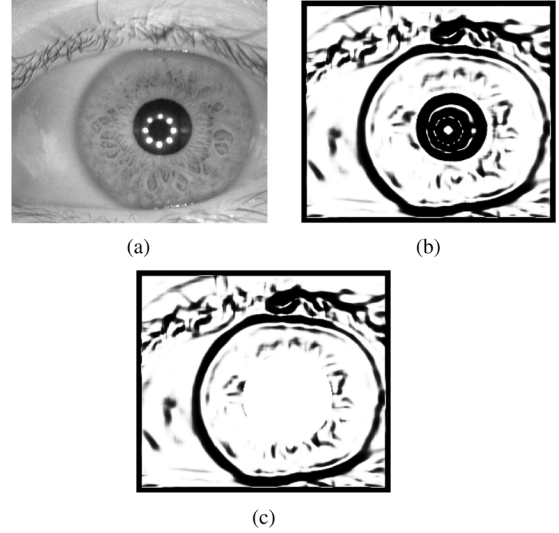
$$\psi_t = -K(c + \epsilon \kappa) \|\nabla \psi\| + \nabla \psi \cdot \nabla K \quad (3)$$

where K , the stopping term for the evolution, is an image dependant force and is used to decelerate the evolution near the boundaries; c is the velocity of the evolution; ϵ indicates the degree of smoothness of the level sets; and κ is the curvature of the level sets computed as

$$\kappa = - \frac{\psi_{xx}\psi_y^2 - 2\psi_{xy}\psi_x\psi_{yy} + \psi_{yy}\psi_x^2}{(\psi_x^2 + \psi_y^2)^{\frac{3}{2}}}$$

where ψ_x is the gradient of the image in the x direction; ψ_y is the gradient in the y direction; ψ_{xx} is the second-order gradient in the x direction; ψ_{yy} is the second-order gradient in the y direction; and ψ_{xy} is the second-order gradient, first in the x direction and then in the y direction. Equation (3) is the level set representation of the GAC model. This means that the level-set C of ψ is evolving according to

$$C_t = K(c + \epsilon \kappa) \vec{N} - (\nabla K \cdot \vec{N}) \vec{N} \quad (4)$$


 Fig. 11. Stopping function for the GACs. (a) Original iris image. (b) Stopping function K . (c) Modified stopping function K' .

where \vec{N} is the normal to the curve. The first term ($\kappa \vec{N}$) provides the smoothing constraints on the level sets by reducing the total curvature of the level sets. The second term ($c \vec{N}$) acts like a balloon force [31] and it pushes the curve outward towards the object boundary. The goal of the stopping function is to slow down the evolution when it reaches the boundaries. However, the evolution of the curve will terminate only when $K = 0$, i.e., near an ideal edge. In most images, the gradient values will be different along the edge, thus, necessitating different K values. In order to circumvent this issue, the third geodesic term ($(\nabla K \cdot \vec{N})$) is necessary so that the curve is attracted toward the boundaries (∇K points toward the middle of the boundary). This term makes it possible to terminate the evolution process even if (a) the stopping function has different values along the edges, and (b) gaps are present in the stopping function.

The stopping term used for the evolution of level sets is given by

$$K(x, y) = \frac{1}{1 + \left(\frac{\|\nabla(G(x, y) * I(x, y))\|}{k} \right)^\alpha} \quad (5)$$

where $I(x, y)$ is the image to be segmented, and k and α are constants. As can be seen, this term $K(x, y)$ is not a function of t .

2) *Iris Segmentation Using GACs*: Consider an iris image to be segmented as shown in Fig. 11(a). The stopping function K obtained from this image is shown in Fig. 11(b) (In our implementation, for WVU nonideal images, $k = 2.8$ and $\alpha = 8$). As the pupil segmentation is done prior to segmenting the iris, the stopping function K is modified by deleting the circular edges because of the pupillary boundary, resulting in a new stopping function K' . This ensures that the evolving level set is not terminated by the edges of the pupillary boundary [Fig. 11(c)].

A contour is first initialized near the pupil [Fig. 12(a)]. The embedding function ψ is initialized as a signed distance function to $\gamma(t = 0)$ which looks like a cone [Fig. 12(b)]. Discretizing

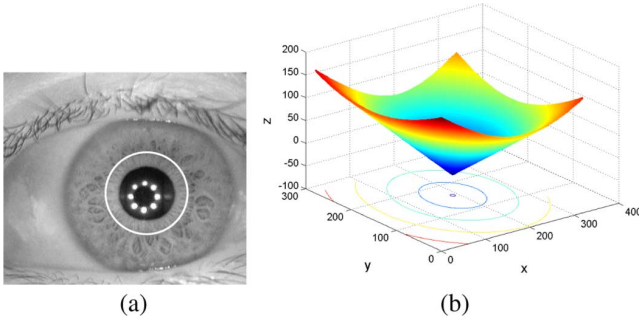


Fig. 12. Contour initialization for iris segmentation. (a) Zeroth level set (initial contour). (b) Mesh plot of the signed distance function ψ .

(3) leads to the following equation:

$$\frac{\psi_{i,j}^{t+1} - \psi_{i,j}^t}{\Delta t} = -cK'_{i,j} \|\nabla\psi^t\| - K'_{i,j} (\epsilon\kappa_{i,j}^t \|\nabla\psi^t\|) + \nabla\psi_{i,j}^t \cdot \nabla K'_{i,j} \quad (6)$$

where Δt is the time step. In our implementation, Δt is set to 0.05. The first term ($cK'_{i,j} \|\nabla\psi^t\|$) on the right-hand side of the above equation is the velocity term (advection term) and in the case of iris segmentation, acts as an inflation force. This term can lead to singularities and, hence, is discretized using upwind finite differences [32]. The upwind scheme for approximating $\|\nabla\psi\|$ is given by

$$\|\nabla\psi\| = \sqrt{A} \\ A = \min(D_x^- \psi_{i,j}, 0)^2 + \max(D_x^+ \psi_{i,j}, 0)^2 \\ + \min(D_y^- \psi_{i,j}, 0)^2 + \min(D_y^+ \psi_{i,j}, 0)^2$$

where $D_x^- \psi$ is the first-order backward difference of ψ in the x-direction; $D_x^+ \psi$ is the first-order forward difference of ψ in the x-direction; $D_y^- \psi$ is the first-order backward difference of ψ in the y-direction; and $D_y^+ \psi$ is the first-order forward difference of ψ in the y-direction. The second term ($K'_{i,j} (\epsilon\kappa_{i,j}^t \|\nabla\psi^t\|)$) is a curvature based smoothing term and can be discretized using central differences. In our implementation, $c = 0.65$ and $\epsilon = 1$ for all iris images. The third geodesic term ($\nabla\psi_{i,j}^t \cdot \nabla K'_{i,j}$) is also discretized using the central differences.

After evolving the embedding function ψ according to (6), the curve starts to grow until it satisfies the stopping criterion defined by the stopping function K' . But at times, the contour continues to evolve in a local region of the iris where the stopping criterion is not strong. This leads to overevolution of the contour. To avoid it, we minimize the Thin Plate Spline energy of the contours. Thin Plate Spline [33] is an interpolation method that finds the minimal “bending energy” to pass a smooth surface through a set of given points. The name “Thin Plate Splines” can be thought of as a simulation of how a thin metal plate would bend if it was forced through some fixed control points. Thus, the thin plate spline energy to pass a smooth surface through coplanar points will be zero where as if the points are nonplanar, the thin plate spline energy will increase with the distance between these points. In this work, Thin Plate Splines are used for minimizing the energy of the contour so as to prevent the

contour from evolving in a highly nonuniform manner. Here, the evolving contour can be thought of as the smooth surface which needs to be fitted through the points on the iris boundary. Thus, if all points on the contour lie on a circle, then the thin plate spline energy will be zero; however, if the contour starts evolving nonuniformly, the thin plate spline energy to fit the contour through these points will start increasing. By computing the difference in energy between two successive contours, the evolution scheme can be regulated. If the difference between the contours is less than a threshold (indicating that the contour evolution has stopped at most places), then the contour evolution process is stopped. In our implementation, this threshold is set to 1. The evolution of the curve and the corresponding embedding functions are illustrated in Fig. 13.

If the Thin Plate Spline energy of the level sets is not minimized, the contour might continue evolving if the stopping function does not have a high magnitude. In such cases, the contour will incorrectly encompass some portion of the sclera inside the final contour as shown in Fig. 14(a). Minimizing the thin plate spline energy of level sets yields a more precise contour of the iris boundary [Fig. 14(b)].

One important feature of GACs is their ability to handle “splitting and merging” boundaries. This is especially important in the case of iris segmentation since the radial fibers may be thick in some portions of the iris, or the crypts present in the ciliary region may be unusually dark, leading to prominent edges in the stopping function. If the segmentation technique is based on parametric curves (e.g., the snakes segmentation technique [34]), then the evolution of the curve might terminate at these local minima. However, GACs are able to split at such local minima and merge again. Thus, they are able to effectively deal with the problems of local minima thereby ensuring that the final contour corresponds to the true iris boundary (Fig. 15).

Since, during the evolution process, the primary interest is only in the zeroth level set of ψ , the embedding function can be evolved only in a narrow band around the zeroth level set [25]. This accelerates the evolution procedure dramatically and, hence, the whole localization and normalization process takes less than a second in a C++ environment. During the evolution process, the contour is evolved around a small narrow band around the contour. The evolution process is not uniform across the contour but can vary due to obstacles such as specular reflections, eyelashes, etc. Thus, after a few iterations the embedding function may not remain a signed distance function and will become “badly conditioned.” So after every few iterations the embedding function is reinitialized by recomputing the embedding function as a signed distance function from the new contour.

The extracted contour is employed to create the binary mask that is used during the matching of the iriscodes (II). To normalize the iris and convert it to a rectangular entity, its radius and the corresponding center coordinates have to be estimated. If the occlusion due to the upper or lower eyelids is substantial, then a circle that fits all the points on the extracted contour will lie inside the actual boundary of the iris. Thus, only those points on the contour lying on the boundary of the iris and sclera (as opposed to the iris and the eyelids) should be used to estimate the radius and center of the iris. To ensure this, six points at

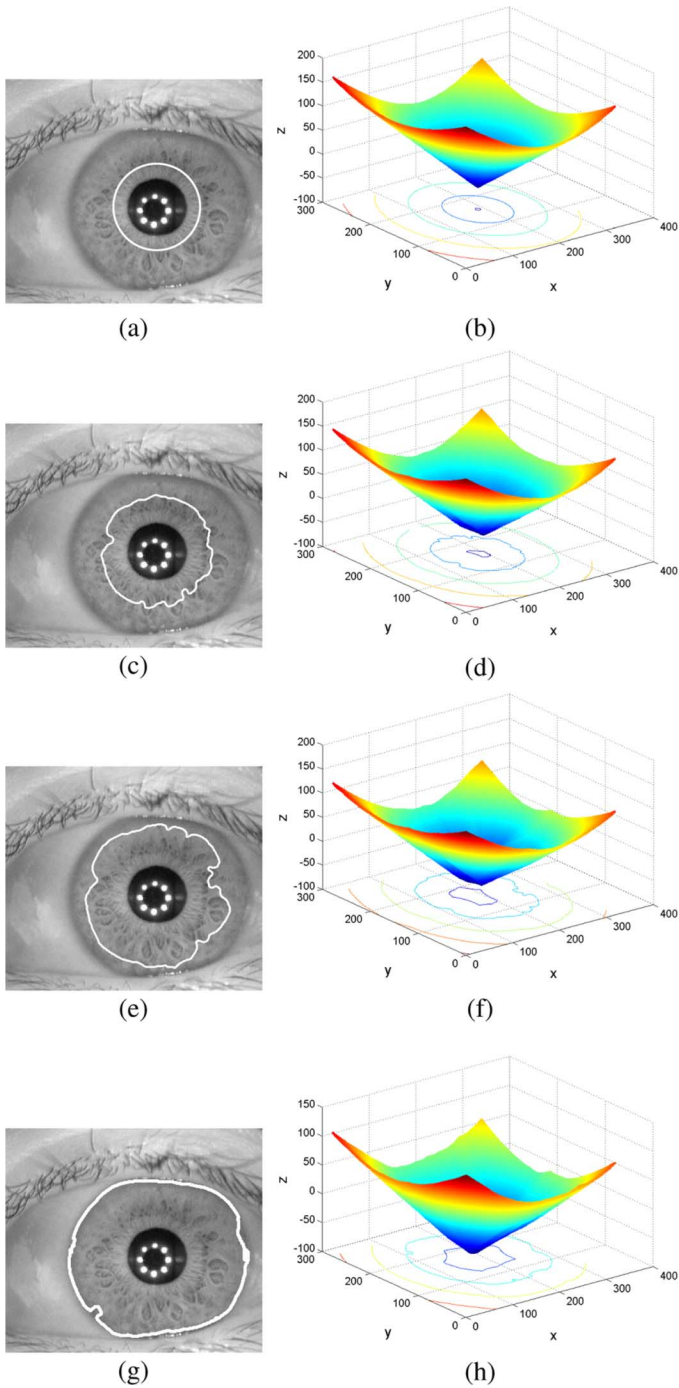


Fig. 13. Evolution of the GAC during iris segmentation. (a) Iris image with initial contour. (b) Embedding function ψ (X and Y axis correspond to the size of the iris image and the Z axis represents different level sets). (c), (d), (e), (f) Contours after 600 and 1400 iterations, and their corresponding embedding functions. (g), (h) Final contour after 1800 iterations and the corresponding embedding function (contours shown in white).

angles of $[-30^\circ, 0^\circ, 30^\circ, 150^\circ, 180^\circ, 210^\circ]$ with respect to the horizontal axis are selected from the extracted contour and their mean distance from the center of the pupil is computed. This value is used as the approximate radius of the iris (R). A circle is next fitted through all the points on the contour that are within a distance of $R \pm 10$ pixels from the center of the pupil. The center and radius of such a circle is the center (x, y) and the

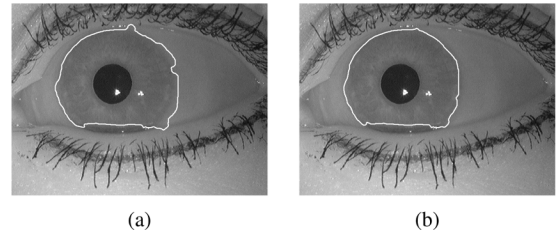


Fig. 14. Effect of minimizing the thin plate energy of the level sets on the evolution of the GAC. (a) Contour without minimizing the thin plate energy of the level sets. (b) Contour obtained by minimizing the thin plate energy of the level sets (contours shown in white).

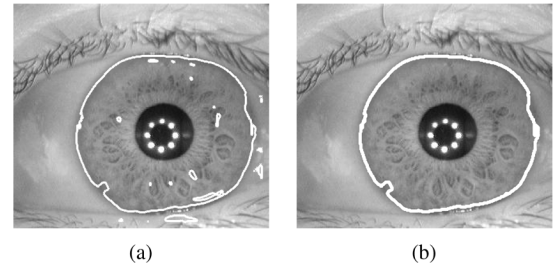


Fig. 15. Final contour segmenting the iris. (a) Geodesic contour splitting at various local minima. (b) Final contour (contours shown in white).

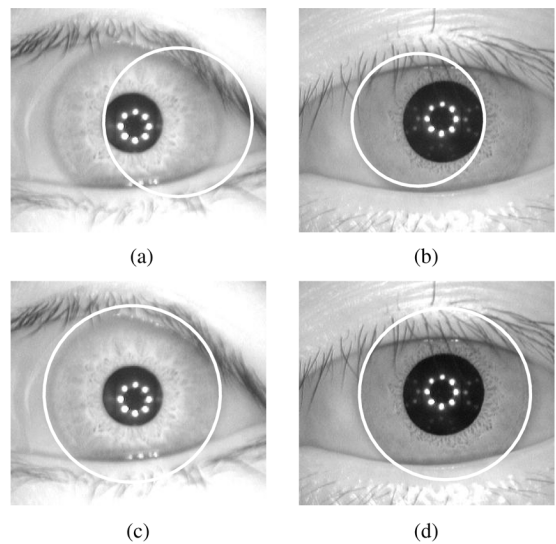


Fig. 16. Robust estimation of the radius and center of the iris using GAC. (a) and (b) Iris center and radius estimated using Masek's algorithm. (c) and (d) Iris center and radius estimated using GACs (iris radius shown in white).

radius R of the iris. Fig. 16 illustrates the radius of the iris detected by our approach along with the radius of the iris detected using the classical integro-differential operators.

When the iris is detected in the corner of the eye, all six points chosen to estimate the approximate iris radius may not lie on the iris boundary; instead some may lie on the eyelid. As the eyelid boundary is closer to the center of the pupil, the approximate iris radius is skewed and is smaller than the actual radius [as shown in Fig. 17(a) and (b)].

As can be seen from Fig. 17(c), the area under the segmented iris curve on either side of the vertical axis passing through the pupil is not equal. The region with smaller area corresponds to the portion where the iris is heavily occluded by the eyelids.

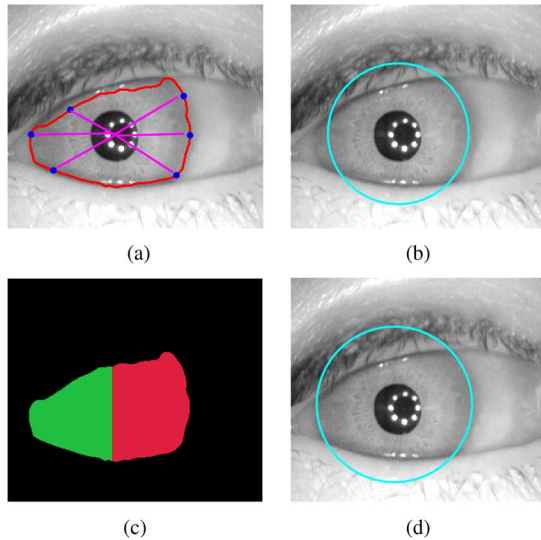


Fig. 17. Iris radius estimation. (a) Iris segmented using GACs; the points used to estimate the iris radius are shown in blue. (b) Estimated iris radius. (c) The area under the curve on either side of the vertical axis passing through the pupil center. (d) Estimated iris radius using only three points lying on the contour corresponding to the larger area.

Hence, whenever the difference between the two areas is more than 10%, only three points lying on the contour corresponding to the larger area are selected to estimate the iris radius. This yields a better estimate of the iris radius and improves the accuracy when the iris is off axis with respect to the camera and relegated to the corner of the eye.

The iris is then normalized using the standard procedure as described in [4] and preprocessed using the Perona–Malik [35] anisotropic nonlinear diffusion algorithm. The anisotropic diffusion equation of an image I can be written as $I_t = \text{div}(g(\nabla I)\nabla I)$ where, the edge descriptor $g(\nabla I)$ controls the degree of smoothing at each point in the image I and is given by $g(\nabla I) = (1)/(1 + ((\|\nabla I\|)/(k))^{\alpha+1})$ ($\alpha > 0$)

Here k and α are constants.³ From the above equation, it is clear that whenever there is no edge in the image, the $g(\nabla I)$ function will approach unity and will act as an isotropic heat diffusion equation, whereas at the locations where edges are present the value of $\|\nabla I\|$ value will be large and the $g(\nabla I)$ function will be nearly zero causing the edge information to be retained. By applying the anisotropic diffusion algorithm, the noise in the image is expected to be reduced. The enhanced output image is then subjected to histogram equalization. Fig. 18(c) shows the normalized image after applying Perona–Malik anisotropic diffusion and histogram equalization.

IV. EXPERIMENTAL RESULTS

The matching performance of our segmentation algorithm was evaluated on the WVU nonideal and CASIA V3-Interval [36] iris image database. The WVU nonideal iris database has

³In our experiments, k is dynamically found such that 90% of the pixels have gradient magnitude less than k , and $\alpha = 1$.

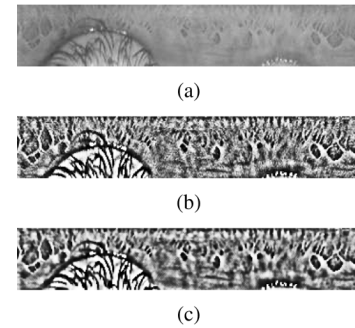


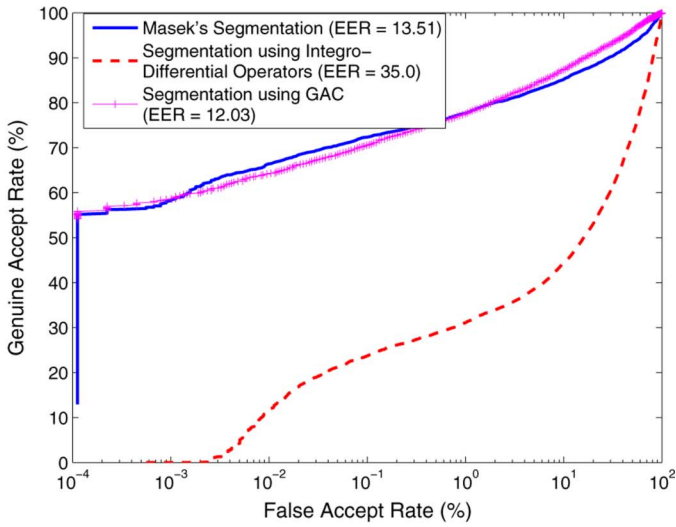
Fig. 18. Perona–Malik anisotropic diffusion. (a) Normalized iris image. (b) Normalized iris image enhanced using histogram equalization. (c) Normalized iris image enhanced using anisotropic diffusion and histogram equalization.

the left (“ L ”) and right (“ R ”) irides of 207 individuals.⁴ There are between 4–15 images of the left and right irides of each individual. The total number of images in the WVU nonideal iris database is 2 678. Each image is of size 640×480 pixels. The performance of GACs was compared with two other iris segmentation techniques: the integro-differential operator and Masek’s segmentation technique [37]. The encoding and normalization of the iris was then carried out using the algorithm as described in Section II.

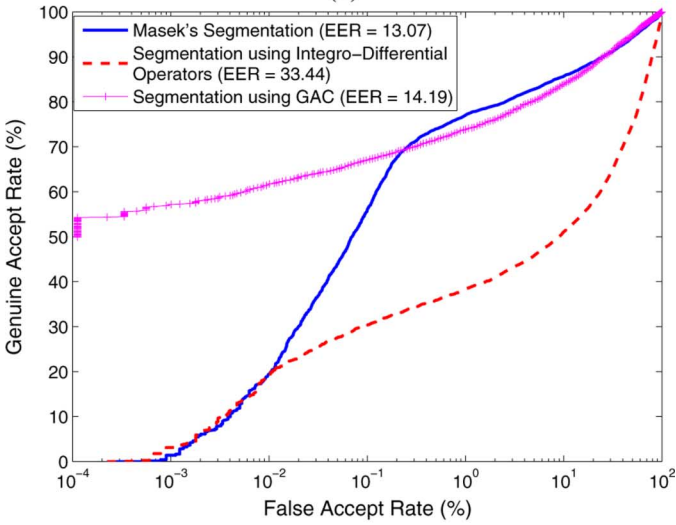
The Receiver Operating Characteristic (ROC) curves for the WVU nonideal *right*-iris database [Fig. 19(a)] indicate that performance does not improve by segmenting irides using GACs (when compared against Masek’s segmentation). But a significant performance gain is achieved by segmenting the WVU nonideal *left*-iris database using GACs [Fig. 19(b)]. For example, the GAR at a fixed FAR of 0.001% using the GAC technique is 58% while that using Masek’s segmentation is 1% and using integro-differential operators is 3%. The phenomenon of one eye performing better than the other has been observed even in the ICE 2005/2006 database. While many reasons have been offered for this discrepancy, researchers are still investigating this phenomenon. In the case of the WVU database, we speculate that the image acquisition protocol has a role to play. If the left iris is captured first, the subject may get used to the acquisition process and thus be able to present the right eye in a fashion that results in better image quality (or vice-versa). However, it must be noted that the proposed technique demonstrates consistent performance across both the eyes unlike Masek’s method.

The CASIA V3-Interval iris database has the left (“ L ”) and right (“ R ”) irides of 249 individuals and 396 eyes. The iris images are of size 320×280 and have approximately 220 pixels across the iris diameter. Most of the images were captured in two sessions, with at least one month interval between the two sessions. There are between 0–20 images of both the left and right irides of each individual. The total number of images in the iris database is 2 655. Three techniques, *viz.*, GACs, integro-differential operators, and Masek’s segmentation technique [37] were used to segment the iris. The normalization and encoding of the iris was then carried out using the technique described in Section II. An additional experiment was performed where the

⁴This is an actively expanding database and, hence, the number of classes is dynamic.



(a)



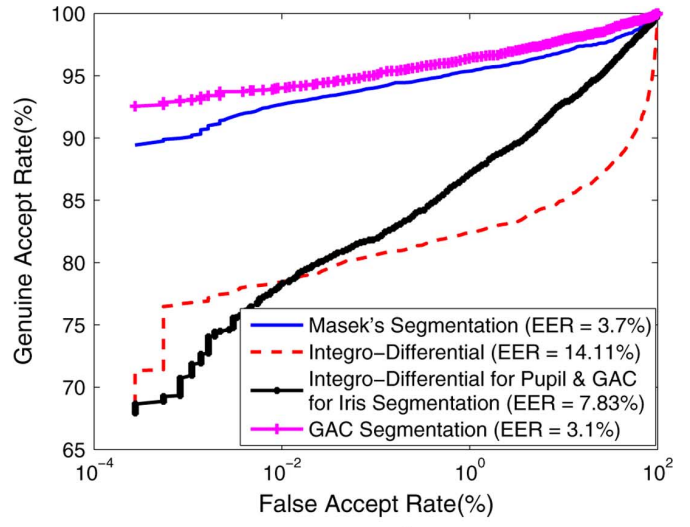
(b)

Fig. 19. Receiver Operating Characteristics of iris recognition on the WVU nonideal iris database. (a) Right iris. (b) Left iris.

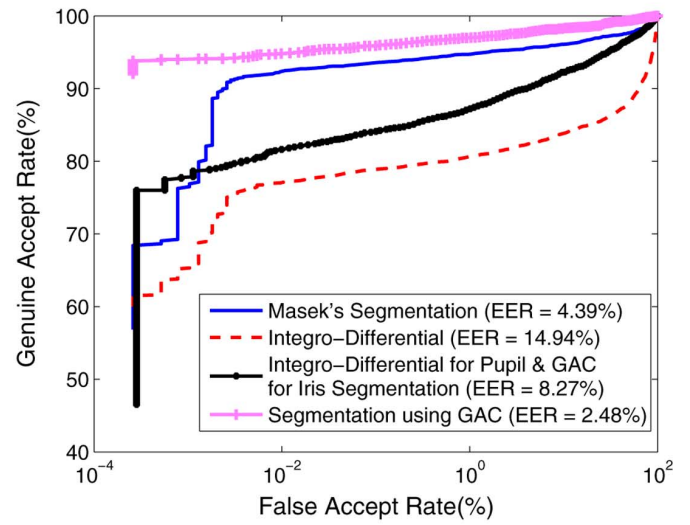
pupil was segmented using integro-differential operators and the iris was segmented using the GAC.

The ROC curves for CASIA V3-Interval *left* and *right* iris database [Fig. 20(a) and (b)] indicate that significant performance improvement is achieved at low FARs by segmenting the irides using GACs. The results are compared against integro-differential operators and Masek's segmentation technique. For example, in the CASIA V3-Interval *left* iris database, the GAR at a FAR of 0.001% using GACs is 94% while that using Masek's segmentation is 69% and using integro-differential operators is 65%. Also, for the CASIA V3-Interval *right* iris database, the GAR at a FAR of 0.001% using GACs is 93% while that using Masek's segmentation is 90% and using integro-differential operators is 77%. Note that the iris segmentation algorithm developed by He *et al.* [38] results in a GAR of 98.5% at a FAR of 0.001% on this database.

We notice that in the case of both databases, the performance using Masek's segmentation is substantially different between



(a)



(b)

Fig. 20. Receiver Operating Characteristics of iris recognition on the CASIA V3 Interval iris database. (a) Right iris. (b) Left iris.

the left and right irides while the GAC scheme is relatively robust and yields the best performance. We also note that (in the case of CASIA V3-Interval database) the iris recognition performance was better when both the pupil and the iris were segmented using our technique (compared to when the pupil was segmented using the integro-differential operators and iris segmentation was done using GAC). In our experiments, the performance of the integro-differential operators is poor compared to Masek's method and the GAC technique. Even though the Daugman implementation of integro-differential operators and active contours is expected to perform much better, we do not have access to these codes and hence could not compare them against our technique. The CASIA algorithm [38] seems to perform better than the GAC. But since the purpose of this paper was to propose a new iris segmentation scheme, we used a relatively simple encoding technique as described in Section II and this may be one of the reasons for the difference between the performances.

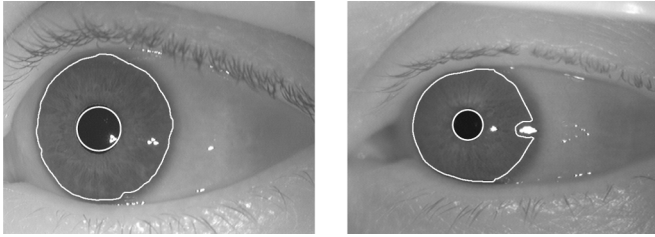


Fig. 21. Segmenting WVU off-angle irides using GAC.

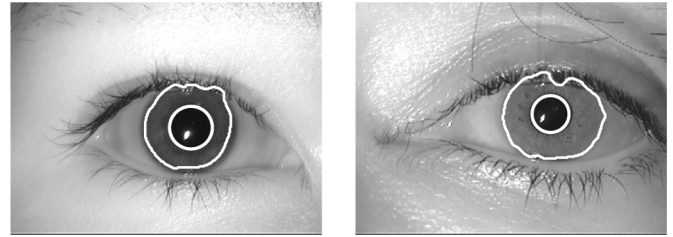


Fig. 23. Segmenting MMU1 irides using GAC.

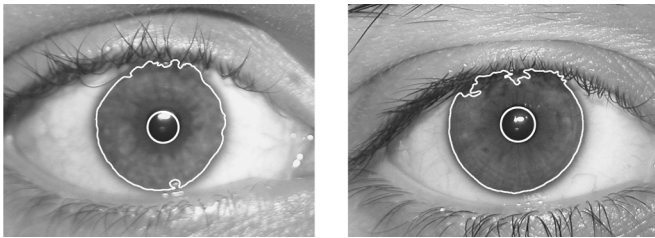


Fig. 22. Segmenting UBIRIS irides using GAC.

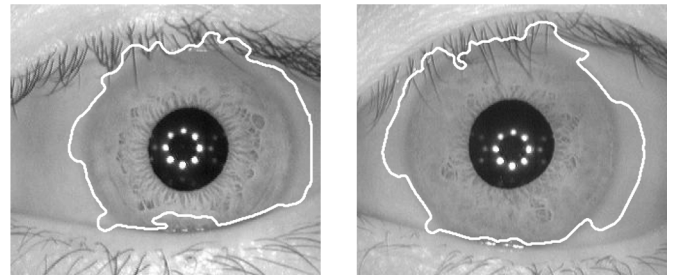


Fig. 24. Over segmented iris images using GAC.

The proposed pupil and iris segmentation algorithms were also used to segment the irides present in other databases such as the UBIRIS database [39] and the MMU1 iris database [40]. The UBIRIS database (session one) was assembled in two separate sessions. A Nikon *E5700* camera was used to capture RGB color images. Each image is of size 800×600 pixels. 241 subjects participated in the first session when 5 images per eye were taken. Only 132 of the 241 subjects participated in the second session and again 5 images per eye were obtained. Thus, the database consists of a total of 1 877 iris images. The MMU1 iris database was captured using a LG IrisAccess[®]2200 camera. It consists of iris images of 45 subjects. 5 images each of the left and the right eyes were taken for every individual resulting in a total of 450 iris images corresponding to 90 classes. The dimensions of each image is 320×280 pixels.

All the images in the UBIRIS dataset (session one) were subjected to the GAC segmentation routine and the results were visually evaluated to determine the accuracy of segmentation. The technique correctly segmented 56.6% of the images (682 images), was slightly off on 7.6% of images (92 images) and could not segment 35.8% of the images (431 images).⁵ The segmentation results on samples from the WVU off-angle, UBIRIS and MMU1 databases can be seen in Figs. 21, 22 and 23, respectively.

V. SUMMARY AND FUTURE WORK

The process of segmenting the iris plays a crucial role in iris recognition systems. Traditionally, iris systems have employed the integro-differential operator or its variants to localize the spatial extent of the iris. In this paper, a novel scheme using GAC for iris segmentation, has been discussed. The GAC scheme is an evolution procedure that attempts to elicit the limbic boundary of the iris as well as the contour

⁵UBIRIS.v2 (session 2) iris images were captured in the visible spectrum unlike irides in other databases which were captured in the near-infrared spectrum. We are still working to make the segmentation scheme suitable for iris images captured in the visible spectrum.

of the eyelid in order to isolate the iris texture from its surroundings. Experimental results on the WVU nonideal and the CASIA V3-Interval datasets indicate the benefits of the proposed algorithm. The algorithm also aids in accurately estimating the radius of the iris and its center. Since active contours can assume any shape and can segment multiple objects simultaneously, the proposed approach mitigates some of the concerns associated with the traditional models. In the literature, the integro-differential operators (Hough transforms) are believed to be more robust for pupil segmentation. However, it must be noted that the technique used in this paper for segmenting the pupil is suitable for operating on the iris images of different databases (CASIA V3, WVU nonideal, UBIRIS, etc.). Integro-differential operators for pupil segmentation are also inherently slower than the approach used in this paper due to the need for fitting circles with varying radii and center coordinates on the image.

The stopping criterion for the evolution of GACs is image independent and does not take into account the amount of edge details present in an image. Thus, if the iris edge details are weak, the contour evolution may not stop at the desired iris boundary leading to an oversegmentation of the iris as shown in Fig. 24. Oversegmentation can be avoided by developing an adaptive stopping criterion for the evolution of the GACs.

In the future, the center of the iris and its radius can be coarsely estimated using a faster technique and the GAC may be initialized near the estimated iris boundary to determine the exact shape of the iris. This will make the current implementation much faster and, therefore, suitable in operational environments. The segmentation process can also be accelerated by using a multiresolution approach. The evolution process can be first initiated on a low-resolution image and an approximate boundary determined. This boundary can be refined by using higher resolution images. This will significantly increase the segmentation speed and will be computationally efficient.

Currently, we are looking at ways to enhance recognition performance in the presence of noise. Specifically, the structure of noise in an iris image could be indicative of the reflective properties of the various components of the iris. We hope to exploit this property during the feature extraction and matching phases of the iris recognition algorithm.

ACKNOWLEDGMENT

This work was performed while S. Shah was with West Virginia University, Morgantown.

REFERENCES

- [1] L. Flom and A. Safir, "Iris recognition system," U.S. Patent 4641349, Feb. 03, 1987.
- [2] K. Bowyer, K. Hollingsworth, and P. Flynn, "Image understanding for iris biometrics: A survey," *Comput. Vision Image Understand.*, vol. 110, no. 2, pp. 281–307, 2008.
- [3] J. Daugman, "New methods in iris recognition," *IEEE Trans. Syst., Man, Cybern.*, vol. 37, no. 5, pt. B, pp. 1167–1175, 2007.
- [4] J. G. Daugman, "High confidence visual recognition of persons by a test of statistical independence," *IEEE Trans. Pattern Anal. Mach. Intell.*, vol. 15, no. 11, pp. 1148–1160, Nov. 1993.
- [5] J. G. Daugman, "Demodulation by complex-valued wavelets for stochastic pattern recognition," *Int. J. Wavelets, MultiResol. Inf. Process.*, vol. 1, no. 1, pp. 1–17, Jan. 2003.
- [6] R. P. Wildes, "Iris recognition: An emerging biometric technology," *Proc. IEEE*, vol. 85, no. 9, pp. 1348–1363, Sep. 1997.
- [7] L. Masek, "Recognition of human iris patterns for biometric identification," B.S. dissertation, The School of Computer Science and Software Engineering, The University of Western Australia, Crawley WA, Perth, Australia, 2003.
- [8] L. Ma, Y. Wang, and T. Tan, "Iris recognition using circular symmetric filters," in *Proc. 16th Int. Conf. Pattern Recogn. (ICPR)*, Quebec City, Canada, Aug. 2002, vol. 2, pp. 805–808.
- [9] S. Lim, K. Lee, O. Byeon, and T. Kim, "Efficient iris recognition through improvement of feature vector and classifier," *J. Electron. Telecommun. Res. Inst.*, vol. 33, no. 2, pp. 61–70, Jun. 2001.
- [10] L. Ma, T. Tan, and Y. Wang, "Efficient iris recognition by characterizing key local variations," *IEEE Trans. Image Process.*, vol. 13, no. 6, pp. 739–750, Jun. 2004.
- [11] J. Huang, L. Ma, Y. Wang, and T. Tan, "Iris model based on local orientation description," in *Proc. Asian Conf. Comput. Vision*, Korea, Apr. 2004, pp. 954–959.
- [12] X. Yuan and P. Shi, "Iris feature extraction using 2-D phase congruency," in *Proc. Third Int. Conf. Inf. Technol. Appl. (ICITA)*, Sydney, Australia, Jul. 2005, vol. 33, pp. 437–441.
- [13] V. Dorairaj and N. Schmid, "Performance evaluation of iris based recognition system implementing PCA and ICA techniques," in *Proc. SPIE Conf. Biometric Technol. Human Identif.*, Mar. 2005, pp. 51–58.
- [14] J. Thornton, M. Savvides, and B. V. Kumar, "Robust iris recognition using advanced correlation techniques," in *Proc. Second Int. Conf. Image Anal. Recogn. (ICIAR)*, Toronto, Canada, Sep. 2005, vol. 3656, pp. 1098–1105, Springer Berlin/Heidelberg.
- [15] J. Huang, Y. Wang, T. Tan, and J. Cui, "A new iris segmentation method for recognition," in *Proc. 17th Int. Conf. Pattern Recogn. (ICPR)*, Cambridge, U.K., Aug. 2004, vol. 3, pp. 23–26.
- [16] A. Abhyankar and S. Schuckers, "Active shape models for effective iris segmentation," in *Proc. SPIE Conf. Biometric Technol. Human Identif. III*, Orlando, FL, Apr. 2006, pp. 62020H.1–62020H.10.
- [17] K. P. Hollingsworth, "Sources of error in iris biometrics," Master's thesis, Graduate School of Comput. Sci. Eng., Univ. Notre Dame, Notre Dame, IN, 2008.
- [18] W. Boles and B. Boashash, "A human identification technique using images of the iris and wavelet transform," *IEEE Trans. Signal Process.*, vol. 46, no. 4, pp. 1185–1188, Apr. 1998.
- [19] K. Bae, S. Noh, and J. Kim, "Iris feature extraction using independent component analysis," in *Proc. 4th Int. Conf. Audio and Video Based Biometric Person Authentic. (AVBPA)*, Guildford, U.K., 2003, pp. 838–844.
- [20] V. Dorairaj, N. A. Schmid, and G. Fahmy, "Performance evaluation of iris based recognition system implementing PCA and ICA encoding techniques," in *Proc. SPIE Conf. Biometric Technol. Human Identif. III*, Orlando, FL, Apr. 2005.
- [21] Z. He, Z. Sun, T. Tan, X. Qiu, C. Zhong, and W. Dong, "Boosting ordinal features for accurate and fast iris recognition," in *Proc. IEEE Comput. Soc. Workshop Biometrics at the Computer Vision Pattern Recogn. Conf.*, 2008.
- [22] Z. He, T. Tan, Z. Sun, and X. Qiu, "Toward accurate and fast iris segmentation for iris biometrics," *IEEE Trans. Pattern Anal. Mach. Intell.*, vol. 31, no. 9, pp. 1670–1684, Jul. 2009.
- [23] L. Zhukov, K. Museth, D. Breen, R. Whitaker, and A. Barr, "Level set modeling and segmentation of DT-MRI brain data," *J. Electron. Imag.*, vol. 12, no. 1, pp. 125–133, Jan. 2003.
- [24] D. Magee, A. Buliplt, and E. Berry, "Level set methods for the 3-D segmentation of abdominal aortic aneurysms," in *Proc. Med. Image Understand. Anal.*, 2001, pp. 141–144.
- [25] R. Malladi, J. A. Sethian, and B. C. Vemuri, "Shape modeling with front propagation: A level set approach," *IEEE Trans. Pattern Anal. Mach. Intell.*, vol. 17, no. 2, pp. 125–133, Feb. 1995.
- [26] W. A. Barrett, Daugman's Iris Scanning Algorithm Biometrics Test Center, San Jose State Univ., Feb. 2000.
- [27] M. Bertalmio, G. Sapiro, V. Caselles, and C. Ballester, "Image inpainting," in *Proc. 27th Ann. Conf. Comput. Graphics Interact. Tech. (SIGGRAPH 2000)*, New York, 2000, pp. 417–424.
- [28] G. Emile-Male, *The Restorers Handbook of Easel Painting.* New York: Van Nostrand Reinhold, 1976.
- [29] J. A. Sethian, "A review of recent numerical algorithms for hypersurfaces moving with curvature dependent speed," *J. Different. Geometry*, vol. 31, pp. 131–161, 1989.
- [30] V. Caselles, R. Kimmel, and G. Sapiro, "Geodesic active contours," *Int. J. Comput. Vision*, vol. 22, no. 1, pp. 61–79, Feb./Mar. 1997.
- [31] L. D. Cohen, "On active contour models and balloons," *Comput. Vision, Graph., Image Process.: Image Understand.*, vol. 53, no. 2, pp. 211–218, 1991.
- [32] J. Sethian and J. Strain, "Crystal growth and dendritic solidification," *J. Computat. Phys.*, vol. 98, pp. 231–253, 1992.
- [33] F. L. Bookstein, "Principal warps: Thin-plate splines and the decomposition of deformations," *IEEE Trans. Pattern Anal. Mach. Intell.*, vol. 11, no. 6, pp. 567–585, Jun. 1989.
- [34] M. Kass, A. Witkin, and D. Terzopoulos, "Snakes: Active contour models," *Int. J. Comput. Vision*, vol. 1, no. 4, pp. 321–331, 1987.
- [35] P. Perona and J. Malik, "Scale-space and edge detection using anisotropic diffusion," *IEEE Trans. Pattern Anal. Mach. Intell.*, vol. 12, no. 7, pp. 629–639, Jul. 1990.
- [36] The CASIA Iris Image Database [Online]. Available: <http://www.sino-biometrics.com>
- [37] L. Masek and P. Kovesi, Matlab Source Code for Biometric Identification System Based on Iris Patterns The School of Comput. Sci. Software Eng., The Univ. Western Australia, 2003 [Online]. Available: <http://www.csse.uwa.edu.au/~pk/studentprojects/libor/source-code.html>
- [38] Z. He, T. Tan, Z. Sun, and X. Qiu, "Robust eyelid, eyelash and shadow localization for iris recognition," in *Proc. ICIP*, 2008, pp. 265–268.
- [39] H. Proena and L. A. Alexandre, "UBIRIS: A noisy iris image database," in *Proc. Int. Conf. Image Anal. Process. (ICIAP)*, 2005, vol. 1, pp. 970–977 [Online]. Available: <http://iris.di.ubi.pt>
- [40] The MMU1 Iris Image Database [Online]. Available: <http://pesona.mmu.edu.my/~ccteo>
- [41] A. Ross and S. Shah, "Segmenting nonideal irises using Geodesic Active Contours," in *Proc. Biometrics Symp. (BSYM)*, Baltimore, MD, Sep. 2006.

Samir Shah received the B.E. degree in electronics engineering from the VIT, Pune, India, in 2002. He received the M.S. degree in electrical engineering from West Virginia University, Morgantown, in 2006. His thesis was on iris segmentation using Geodesic Active Contours.

After receiving the B.E. degree, he was with Siemens Information Systems Ltd., India, as a software engineer working on face recognition algorithms (2002–2003). He is now working as a Software Engineer with the Iris Technology Division, LG Electronics USA Inc., Cranbury, NJ, developing iris recognition algorithms. His research interests include image processing, computer vision, biometrics, and financial markets.

Mr. Shah has served as a Reviewer on National Institute of Justice Research Grant Panels. He presented work on iris image quality at the NIST Biometric Quality Workshop in 2007. He has also served as one of the U.S. experts in iris recognition technology at the ISO/IEC JTC1 SC37 meeting for biometric standards in 2008 and 2009.

Arun Ross (S'00–M'03) received the B.E. (Hons.) degree in computer science from the Birla Institute of Technology and Science, Pilani, India, in 1996, and the M.S. and Ph.D. degrees in computer science and engineering from Michigan State University, East Lansing, in 1999 and 2003, respectively.

Between 1996 and 1997, he was with the Design and Development Group of Tata Elxsi (India) Ltd., Bangalore, India. He also spent three summers

(2000–2002) with the Imaging and Visualization Group of Siemens Corporate Research, Inc., Princeton, NJ, working on fingerprint recognition algorithms. He is currently an Associate Professor in the Lane Department of Computer Science and Electrical Engineering, West Virginia University, Morgantown. His research interests include pattern recognition, classifier fusion, machine learning, computer vision, and biometrics. He is actively involved in the development of biometrics and pattern recognition curricula at West Virginia University. He is the coauthor of the “Handbook of Multibiometrics” and coeditor of the “Handbook of Biometrics.”

Dr. Ross is a recipient of NSF's CAREER Award and was designated a Kavli Frontier Fellow by the National Academy of Sciences in 2006. He is an Associate Editor of the IEEE TRANSACTIONS ON IMAGE PROCESSING and the IEEE TRANSACTIONS ON INFORMATION FORENSICS AND SECURITY.